How Purely Wind-Driven Long Planetary Geostrophic Waves May Be Energized in the Western Part of Ocean Subtropical Gyres

IVANA CEROVEČKI* AND ROLAND DE SZOEKE

College of Oceanic and Atmospheric Sciences, Oregon State University, Corvallis, Oregon

(Manuscript received 22 February 2005, in final form 15 May 2006)

ABSTRACT

Satellite observations and idealized numerical studies reveal intensification of long-period (on the order of one cycle per year) waves in the western part of ocean basins. The authors explore the idea that the intensification is associated with the spatial growth of purely time periodic, but baroclinically unstable, motions. The framework is a simple idealized 2½-layer model in which only the upper layer is directly forced by the wind, a setting similar to the shadow zone of the Luyten–Pedlosky–Stommel (LPS) model. The upper two layers participate in the wave motion, which is driven by a large-scale wind stress fluctuating with the annual period, representing the seasonal cycle. Although possibly unstable solutions exist everywhere in the subtropical gyre on account of the nonzero meridional background flow, they are not seen in the eastern part of the basin in satellite observations nor are they excited there by model gyre-scale annual-period winds. Instead, energy injected into the model ocean at a fixed frequency and with zonal and meridional wavenumbers, such that the resulting flow perturbation is locally stable, refracts westward as it propagates through the spatially varying background flow without change of frequency and reaches distant regions where the spatial wavenumber becomes complex so that spatial growth occurs. This process results in spatially growing solutions of annual or near-annual frequency only in the southwestern part of the model subtropical gyre, thus explaining why the intensification is preferentially manifested in the southwestern subtropical gyre in published numerical model results. The paper concludes with a discussion of relevant satellite and in situ observations.

1. Introduction

Chelton and Schlax (1996) suggested that purely periodic (annual period) wind-driven long planetary waves can become energized in the western part of ocean basins. Explanations of this in the literature generally involve either (i) modification by midocean ridge topography of long waves radiated from the eastern boundary (Barnier 1988; Tailleux and McWilliams 2002) or (ii) baroclinic instability (Liu 1999a; Dewar and Huang 2001; Kubokawa and Nagakura 2002). Osychny and Cornillon (2004) make the point that variance associated with western boundary current variability must also be considered. It is unlikely that any one of these mechanisms is totally unimportant, and each mechanism (ridge modification, baroclinic instability, western boundary current variance) has its own set of complicated spatial signatures. A definitive comparison of available observations with these is desirable but beyond the scope of this paper, which focuses on the second mechanism in the context of a linearized, time-dependent 2½-layer version of the Luyten et al. (1983, hereinafter LPS) ventilated thermocline model. The present results are briefly compared with observations in the concluding section of the paper.

Gill et al. (1974) were the first to suggest, on general grounds, that this southwestern region might be prone to baroclinic instability. Liu (1999a,b), Dewar (1998), and Kubokawa and Nagakura (2002) studied the linear dynamics of perturbations of, respectively, 3-layer and 2½-layer quasigeostrophic (QG) subtropical gyre flow, finding that the unventilated regions of the gyre were unstable to long-wave perturbations. Liu (1999a) perturbed the steady flow of an eddy-resolving three-layer

* Current affiliation: Program in Atmospheres, Oceans, and Climate, Department of Earth, Atmospheric, and Planetary Sciences, Massachusetts Institute of Technology, Cambridge, Massachusetts.

Corresponding author address: Ivana Cerovečki, Room 54-1721, Dept. of Earth, Atmospheric, and Planetary Sciences, Massachusetts Institute of Technology, Cambridge, MA 02139-4307.
E-mail: ivana@rossby.mit.edu

DOI: 10.1175/JPO2977.1

QG ocean model with a spatially uniform Ekman-pumping harmonic at a period of 3 yr. He found the ocean response to periodic (3-yr period) Ekman pumping to be "almost unchanged in longitude until it enters the southwestern part of the subtropical gyre, where linear eigenvalue calculations show the strongest planetary wave instability." The background flow of Liu (1999a) was confined to the upper layer, but Liu (1999b) as well as Dewar and Huang (2001) subsequently found similar results in numerical experiments with a partially ventilated subtropical gyre flow. Liu (1999a) suggested that the amplification in the southwestern subtropical gyre was related to the possibility that "the temporal instability of an eigenmode (complex frequency with real wave number) may correspond to a spatially unstable radiating mode that is forced by a given frequency (real frequency with a complex wavenumber)."

This apparent geographical restriction of the occurrence of instability is in contrast with the subsequent results of Walker and Pedlosky (2002), and more recently the results of Cerovečki and de Szoeke (2006). Walker and Pedlosky (2002) found that, with nonzero purely meridional background flow confined to the upper layer of a two-layer QG model, there is no minimum shear required for instability; for any value of β, arbitrarily small shears will become unstable although the associated growth rates may be small. Nonzero meridional background flow thus dramatically changes the dispersion relation by making the zonal perturbations (which are not stabilized by the β effect) more capable of releasing potential energy of the background flow (Pedlosky 1987). Thus, instability need not be confined to any particular region of the subtropical gyre.

Even for purely zonal background flow in the 2½-layer model, Liu (1999a) pointed out that planetary waves can become unstable in westward flow with sufficient vertical shear. In a westward flow and shear, the mode that propagates most slowly in the absence of background flow (the A mode) is strongly advected westward by the background flow, while the mode that propagates most rapidly in the absence of background flow (the N mode) does so at a speed that is almost insensitive to the background flow. When the westward flow is strong enough for the speed of the A mode to be comparable to that of the N mode, the two waves become coupled and unstable. This mechanism remains important when the background flow has both zonal and meridional components.

These results raise two questions to be answered as the goal of this paper: (i) Why are the time-periodic baroclinically unstable solutions preferentially excited in the southwestern part of the subtropical gyre in published numerical model results, although there are possibly unstable solutions everywhere in the basin, and (ii) is it necessary for baroclinically unstable perturbations to be generated by local forcing or can baroclinically unstable perturbations be generated by remote wind forcing?

A brief summary of the answers is that, although possibly unstable solutions with period on the order of the annual period exist everywhere in the subtropical gyre on account of the nonzero meridional background flow, they occur everywhere at meridional wavenumbers much larger than those characterizing gyre-scale winds. They are consequently not excited over most of the model gyre by gyre-scale winds whose period is on the order of the annual period. Instead, long-wave energy injected into the model ocean at such periods refracts as it propagates westward through the spatially varying background flow without a change of frequency and reaches distant regions where the combination of refractively changed wavenumber and local background flow instability properties results in spatial growth. At annual or near-annual frequencies this occurs only in the southwestern part of the model subtropical gyre, thus explaining why the intensification is preferentially manifested there in published numerical model results.

The remainder of the paper is organized as follows. A time-dependent 2½-layer version of the LPS model linearized about the steady solution is formulated in section 2 and the appendix. The mathematical nature of the model boundary value problem and the method of solution are explained in section 3. A perturbation solution driven by annual period winds that extend over the entire model subtropical gyre displays strong intensification in the southwestern part of the model gyre (Fig. 1). Free-wave periodic perturbation solutions are studied in section 4a. The A and N modes of Liu (1999a) are identified and, as in Liu (1999a), spatial instability manifested by the occurrence of complex wavenumbers takes place in the vicinity of the wavenumber plane at which the stable branches of the A- and N-mode dispersion relations would intersect if extrapolated across the region of instability. Within the simplified framework of a background circulation idealized to vary only in the zonal direction (section 4b), periodic perturbations excited by specified values at the eastern boundary initially propagate westward as A- or N-mode plane waves but then are found to refract into perturbations that grow toward the west. This also occurs when both meridional and zonal variations of the background flow are retained (section 4c). In this case, the resulting free-wave perturbation solutions closely resemble solutions forced by winds blowing over all or

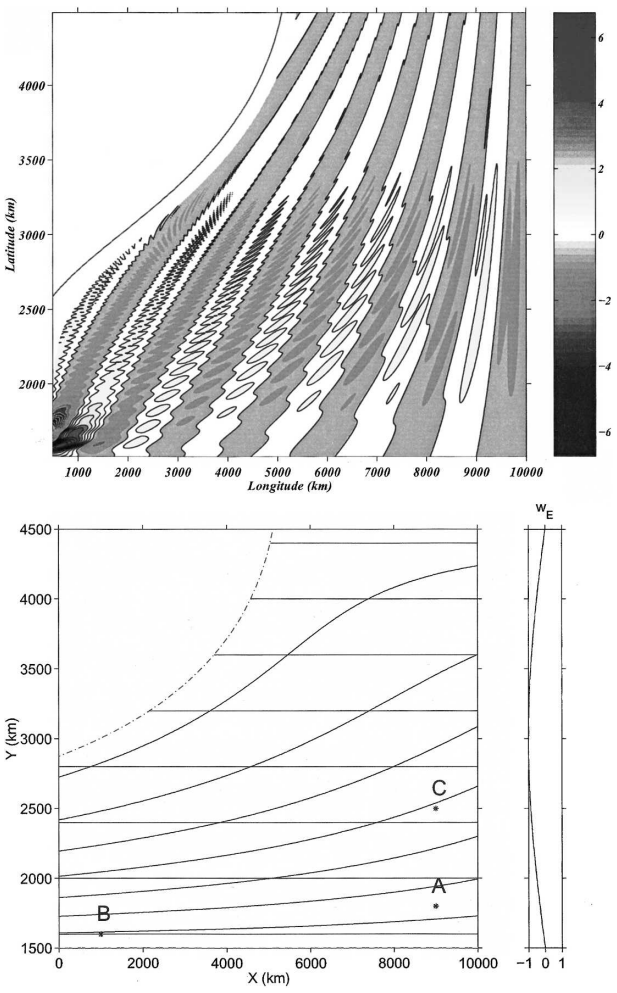

FIG. 1. (top) Snapshot of the annual period interfacial displacement η_2 of the base of the middle layer obtained by solving (1) with annual-period Ekman forcing having the scaled meridional profile shown in the bottom-right panel. The background steady flow is specified by the parameters $H_{10} = 300$ m, $H_{20} = 750$ m, $\gamma_1 = 0.0245$ m s^{-2}, and $\gamma_2 = 0.01$ m s^{-2} and is driven by steady Ekman pumping as described in the appendix, with the meridional profile shown in the bottom-right panel. The western boundary x_B of the shadow zone of the steady circulation is also shown. (bottom) Characteristics of (1) obtained by solving (4) for the annual period. Zonal characteristics are not continued beyond x_B. Points labeled A, B, and C are referenced in Figs. 2 and 3.

only part of the subtropical gyre, meaning that, for the particular wind stress field and boundary geometry of this paper, the contribution of free modes to the directly forced solution is dominant. The paper concludes with a discussion of relevant in situ and satellite observations of long-period Rossby waves.

2. Governing equations

Theories of large-scale ocean flow commonly make use of the planetary geostrophic (PG) approximation in which the open ocean flow is geostrophic, except for a surface Ekman layer. In this paper a 2½-layer PG model governs the wind-driven steady circulation of a subtropical gyre in a rectangular midlatitude basin. We consider small amplitude time-dependent perturbations of such a steady flow that are driven by specified time-dependent surface Ekman pumping $w'_E(x, y, t)$. The equations of the model and the particular steady solution of this paper are given in the appendix. An important feature of the steady solutions considered here is that, since the deeper layers do not surface to be exposed to the wind, the steady flow is confined to the upper layer, a situation analogous to the eastern shadow zone of the LPS model.

The 2½-layer equations for time-dependent perturbations η_1 and η_2 of the upper and lower interfaces between the three fluid layers are [see (A10) and (A11)]

$$\eta_{2t} + U_R\eta_{2x} + V_R\eta_{2y} = \eta_{1t} \quad \text{and}$$
$$\eta_{2t} - c\eta_{2x} - (C\eta_1)_x = w'_E. \tag{1}$$

In these equations, and subsequently, subscripts x, y, and t denote differentiation. For notational simplicity we have introduced the abbreviations

$$C(x, y) \equiv \frac{\beta\gamma_1 H_1^0}{f^2} \quad \text{and} \quad C(y) \equiv \frac{\beta\gamma_2 H_2^0}{f^2} \tag{2}$$

in which H_j^0 is the unperturbed depth of the base of layer j (indices $j = 1, 2, 3$ correspond to the upper, middle, and lower layer, respectively), $f(y)$ is the Coriolis parameter, $\gamma_j = g(\rho_{j+1} - \rho_j)/\rho_0$ ($j = 1, 2$) are reduced gravity parameters, and

$$U_R \equiv \frac{\gamma_2}{\gamma_1}(u_g + c_R) \quad \text{and} \quad V_R \equiv \frac{\gamma_2}{\gamma_1}v_g, \tag{3}$$

where u_g and v_g are the mean upper-layer geostrophic velocity components given by $-\gamma_1 H_{1y}^0/f$ and $\gamma_1 H_{1x}^0/f$ in the zonal x and meridional y directions, and $c_R = C - (\gamma_1/\gamma_2)c$.

3. Characteristic structure and numerical procedure for time-harmonic motions

Shown in Fig. 1 are the two sets of characteristics of the perturbation equations in (1) that are defined by

$$\frac{dy}{dx} = 0 \quad \text{and} \quad \frac{dy}{dx} = \frac{V_R}{U_R}. \tag{4}$$

Characteristics of (1), obtained by solving the first of (4), are zonal lines extending westward from the eastern boundary. The characteristics of (1), obtained by solving the second of (4), are lines of constant middle-

layer potential thickness that bend southwestward away from the eastern boundary; the northernmost of these is the western boundary $x_B(y)$ of the shadow zone of the steady solution. The solution of (1) at some point x, y within the shadow zone is determined by the forcing w'_E over the triangular area between the two characteristics that meet at x, y and extend back to the eastern boundary $x = a$ and by the values of η_1 and η_2 specified at the eastern boundary between the points of intersection of the two characteristics and the eastern boundary.

It is thus clear that η_1 and η_2 in the shadow zone $x_B(y) < x < a$ are fixed by values specified at the eastern boundary and by forcing over the shadow zone. The zonal characteristics cross the boundary x_B and partly determine the solution in the region $x < x_B(y)$ west of the shadow zone, but the entire solution in this region is fixed only when the other set of characteristics, which carry information away from the western boundary of the ocean, is taken into account. In this paper, we restrict our analysis to the shadow zone. A more complete treatment of the boundary value problem including the region beyond x_B is in preparation.

Figure 1 shows a numerical solution of the perturbation equations in (1), with coefficient fields $U_R(x, y)$, $V_R(x, y)$, $C(x, y)$, and $c(y)$ derived from the steady solution of the appendix. The solution of Fig. 1 is excited by an annual period fluctuation of the same large-scale wind stress pattern (Fig. 1) that drove the steady background flow of the appendix. The solution was obtained by making a finite-difference approximation to the y derivative in the first of the forced perturbation equations in (1), and then using an adaptive Runge–Kutta method to integrate the resulting coupled equations westward, with harmonic time dependence, starting from the condition of no normal flow (alongshore constancy of interfacial depths in the PG approximation) at the eastern boundary $x = a$. To avoid numerical difficulties associated with carrying out this integration in a domain of integration whose zonal extent (from the eastern boundary to the western boundary x_B of the shadow zone) is strongly y dependent, the westward integration was carried out in a stretched coordinate χ obtained by first defining $\xi = -a(x - a)/[x_B(y) - a]$ in terms of which $x_B(y)$ is mapped into the straight line $\xi = -a$, and the eastern boundary is at $\xi = 0$, and then making a further logarithmic transformation, $\chi = a\ln(1 + \xi/a)$, in order to increase the resolution close to x_B. In terms of χ, the eastern boundary corresponds to $\chi = 0$ and the western boundary of the shadow zone x_B corresponds to $\chi = -\infty$. The actual integration over χ did not, of course, literally reach $\chi = -\infty$; that is why the solution of Fig. 1 extends to points very close to, but not quite at, the western boundary $x_B(y)$ of the shadow zone.

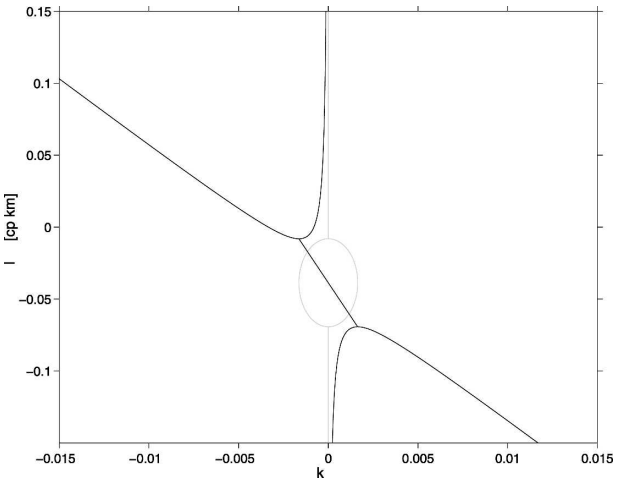

FIG. 2. The dispersion relation (5) obtained for parameters c, C, U_R, and V_R at the location labeled C ($x = 9000$ km, $y = 2500$ km) in Fig. 1 by assuming real meridional wavenumber l and solving for the zonal wavenumber k (real values plotted as heavy lines; imaginary values plotted as light lines). Note that k is real except over a restricted range of meridional wavenumber l. For this range of l, corresponding solutions of (1) grow zonally.

This numerical procedure is efficient enough that meridional grid spacings on the order of a few tenths of a percent of the gyre meridional-scale Δ are readily obtained, and the adaptive Runge–Kutta procedure achieves significantly better zonal resolution than this. The wave fronts in the solutions are nearly meridional near the eastern boundary but increasingly slope from northeast to southwest in the western part of the gyre. The integration fails when the wave front slope becomes the order of or less than the ratio of east–west wavelength to meridional computational grid wavelength: This condition is most restrictive for the short-wave (A mode) solutions. The reason that westward integration is appropriate for this boundary value problem is further discussed in section 4b.

4. Properties of free solutions

a. WKB dispersion relation

Inserting $e^{-i(\sigma t - kx - ly)}$ into the homogeneous version of (1) with constant coefficients yields the Wentzel–Kramers–Brillouin (WKB) dispersion relation

$$\sigma^2 + \sigma(c + C)k - CU_Rk^2 - CV_Rkl = 0. \qquad (5)$$

Figure 2 shows this dispersion relation at the particular location in the model subtropical gyre labeled C in Fig. 1 for the annual period. In this figure, the meridional

wavenumber l has been taken to be real, and the dispersion relation has been solved for the zonal wavenumber k. At point C and elsewhere in the gyre, both real and complex values of k generally result.

The properties of free solutions corresponding to the two roots of the dispersion relation (5) have already been discussed by Liu (1999a,b) and by Kubokawa and Nagakura (2002). The two roots of (5) correspond to the non-Doppler-shift mode N and the advective mode A of Liu (1999a), which reduce to the first (fast) and second (slow) baroclinic mode in the case of no background flow. The N mode propagates westward at all latitudes and the A mode tends to follow the mean flow. In accord with the suggestion of Liu (1999a) noted above, instability as manifested by the occurrence of complex values of k indeed takes place in the vicinity of the meridional wavenumber at which the stable branches of the A-mode and N-mode dispersion relations would intersect if extrapolated across the region of instability.

b. Free waves in zonally varying background flow

How to link stable wave propagation with unstable waves has been a longstanding issue in the literature; significant results are those of Pierrehumbert (1984) and of Pedlosky (1989). Unlike these, the present case is fully two-dimensional, but it also appears to be conceptually simpler. Some insight may be gained from the following simplified problem.

In the idealized case that the coefficients U_R, V_R, C, and c of (1) vary only in the zonal (x) direction, then solutions of (1) periodic in time have the form of functions of x multiplied by $e^{(-i\sigma t+ily)}$ so that (1) become a pair of coupled ordinary differential equations with independent variable x, which may (under conditions to be defined subsequently) be integrated westward. The two interfacial displacements η_1 and η_2 are specified at the easternmost point where the integration starts; l is specified at the eastern boundary. The amplitude of η_2 is there arbitrarily set to unity and the amplitude for η_1 is obtained from either of the unforced equations in (1) by selecting one of the two roots for k from the dispersion relation (5). This gives interfacial displacements that are either in phase with one another with relative amplitudes appropriate to a fast N-mode free wave or are out of phase with one another with relative amplitudes appropriate to a slow A-mode free wave.

Figure 3 shows one solution (corresponding to the A mode) of (1) obtained in this manner for fixed l, σ over a computational domain $0 < x < a$ in which, over the eastern third of the domain, the values of U_R, V_R, C, and c are set equal to those that prevail at point A of Fig. 1 and are set equal to those that prevail at point B of Fig. 1 over the western third of the domain. In the middle third of the domain they are linearly interpolated between their values in the eastern and western thirds of the domain. Points A and B of Fig. 1 are chosen so that at point A the plane wave dispersion relation (5) evaluated with the specified values of σ, l and the local values of U_R, V_R, C, and c yields real values of k, whereas at point B the plane wave dispersion relation (5) evaluated with the specified values of σ, l and the local values of U_R, V_R, C, and c yields complex values of k.

In the eastern third of the domain, plane waves propagate uniformly away from the eastern boundary. In the middle third of the domain, where the values of U_R, V_R, C, and c vary linearly in x, the waves initially lengthen, but then, very close to the point at which that the value of k given by the dispersion relation (5) evaluated for the specified values of σ, l and the locally interpolated values of U_R, V_R, C, and c changes from being real to being complex, the solutions begin to grow westward exponentially and continue to do so in the western third of the domain.

Figure 3 also shows the dispersion relation (5) evaluated at points A and B of Fig. 1. Although l does not change as the solutions propagate westward, the region of zonal instability along the l axis of the dispersion relation both grows in extent and moves upward toward more positive values of l as the parameters U_R, V_R, C, and c vary westward from their values at point A of Fig. 1 to those at point B. Zonal growth of the solution starts at the value of x at which the uppermost point of the region of zonal instability just reaches the value of l characterizing the solution.

Four cases may be distinguished: In every case, conditions at the eastern boundary generate a westward propagating stable wave incoming toward the region of zonal variation of the medium. In analyzing the four cases, it is important to note that, for meridional wavenumbers l greater than the largest positive value of l for which k is complex, there are two propagating waves, both of which have westward group velocity; whereas, for meridional wavenumbers l less than the most negative value of l for which k is complex, there are also two propagating waves, but one (the one with the larger value of k) has westward group velocity while the other has eastward group velocity.

(i) If the meridional component of the wavenumber vector l of the incoming wave is larger than the largest positive value of l for which the solution in the region to the west of the region of medium variability becomes unstable, no reflected waves can be generated because the zonal component of the

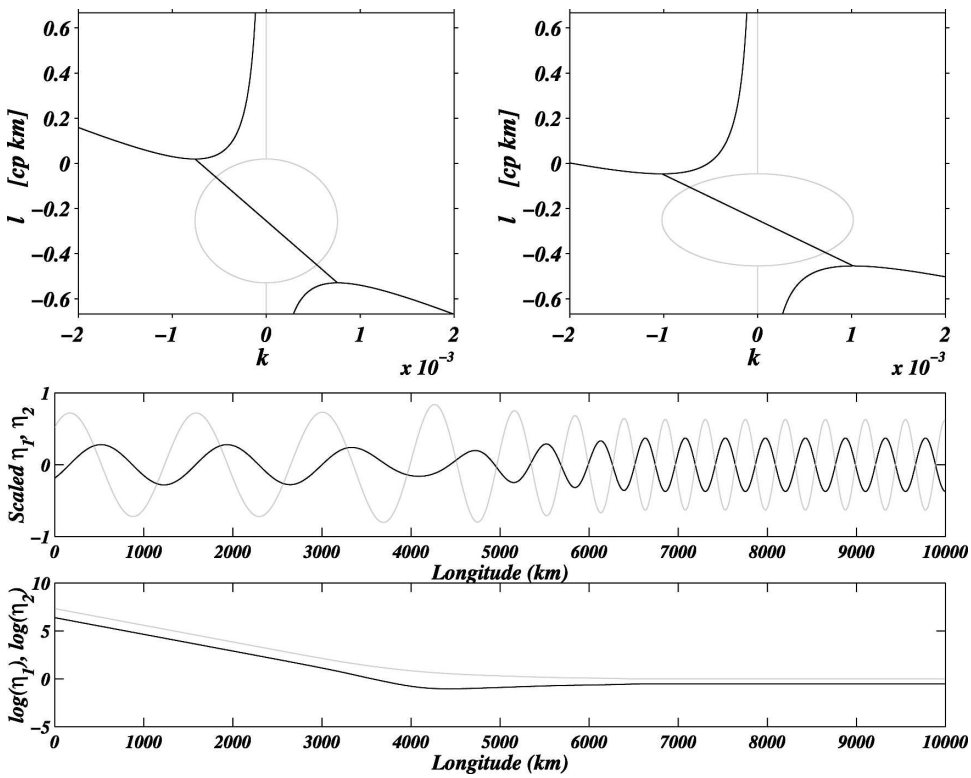

FIG. 3. (top) The dispersion relation (5) obtained for parameters c, C, U_R, and V_R at the locations labeled (left) B and (right) A in Fig. 1 by assuming real meridional wavenumber $l = \pi/\Delta$ and solving for the zonal wavenumber k (real values plotted as solid lines; imaginary values plotted as light lines). The numerical value of l is 1.667×10^{-4} cp km. Note that l falls above the region of zonal growth in the right-hand panel, but falls within the region of zonal growth in the left-hand panel. (middle) Instantaneous plot (against x) of time-variable A-mode interfacial displacements η_1 (light line) and η_2 (solid line), obtained by integrating (1) westward from the eastern boundary $x = a$ with no Ekman pumping but with eastern boundary values of η_1 and η_2 at $x = a$ set as in section 4b and with parameters c, C, U_R, and V_R chosen at their values at the locations labeled B and A in Fig. 1 over $0 < x < a/3$ and $2a/3 < x < 0$, respectively and, within $a/3 < x < 2a/3$, chosen to linearly interpolate between these values. For plotting, η_1 and η_2 are scaled by $(\eta_1^2 + \eta_2^2)^{1/2}$; (bottom) $\log(\eta_1)$ (light line) and $\log(\eta_2)$ (solid line) plotted against x. Note, in the bottom panel, the onset of westward growth in the interval $a/3 < x < 2a/3$; this begins at the value of x at which the uppermost limit of the region of zonal instability in the dispersion relation (5) evaluated for the parameters $c(x)$, $C(x)$, $U_R(x)$, and $V_R(x)$ just reaches the meridional wavenumber $l = \pi/\Delta$ imposed at the eastern boundary.

group velocity is westward for both possible incoming waves. To match both interfacial depths across the region of medium variability two transmitted stable waves are therefore required.

(ii) If the incoming wave has a value of l within the range of l for which both solutions to the east of the region of medium variability have westward group velocities while both solutions west of the region of medium variability grow or decay zonally, then again, because the zonal component of the group velocity is westward for both possible incoming waves, two transmitted solutions will be necessarily generated, one growing westward of the region of medium variability and one decaying westward.

(iii) If the incoming wave has a negative value of l below the range of l for which both solutions to the west of the region of medium variability are unstable, then both eastward and westward of the region of medium variability one wave has eastward group velocity and one has westward group velocity. Consequently, the response to the incoming wave must be a reflected wave propagating eastward and a transmitted wave propagating westward.

(iv) If the incoming stable wave has a value of l within the range of l for which the long-wave solution east of the discontinuity has eastward group velocity and the short-wave solution has westward group

velocity, while both solutions to the west of the discontinuity are unstable, then it might be argued that the response to the incoming wave is a reflected wave propagating eastward from the region of medium variability and a wave decaying westward from the region of medium variability. Such an argument would, however, be incorrect (J. Pedlosky 2005, personal communication; see also course notes available online at http://www.whoi.edu/PO/scientist/biosketch/pedlosky.html). When instability is present, then it is only in the case of very large damping that physically meaningful solutions necessarily decay away from a region of generation (such as the present region of medium variability). Damping is readily included in the dispersion relation (5) by giving the frequency a positive imaginary part, $\sigma \to \sigma + i\mu$ in which $\mu > 0$. For sufficiently large μ, solutions corresponding to both roots of (5) decay westward. Consequently, the "reflected" solution is not allowed eastward of the region of medium variability so that, westward of the region of medium variability, both solutions are required. This remains true as $\mu \to 0$ so that finally in this case the response to the incoming wave is excitation of both the westward growing and westward decaying solutions west of the region of medium variability.

The solutions of Fig. 3 correspond to case ii. Westward integration is correct for cases i, ii, and iv, but not for case iii. All solutions in this paper are for cases i and ii.

c. *Free waves with subtropical gyre background flow*

The annual period N-mode free-wave numerical solution of (1) obtained by the methods of section 3 is shown in Fig. 4. The corresponding solution for the A mode (not shown) is qualitatively similar except that it is characterized by shorter wavelengths. The solutions have been obtained by numerically integrating the homogeneous version of the perturbation equation (1) westward from the eastern boundary with the same specification of η_1 and η_2 there as in the foregoing section. The meridional variation of η_1 and η_2 at the eastern boundary is specified as $\sin[(y - b)\pi/\Delta]$ so that the solutions there are characterized by the meridional wavenumbers $\pm\pi/\Delta$ (where Δ is the meridional width of the basin). This choice is made so that, at least near the eastern boundary, the free solutions will have the same meridional structure as the forced solution of Fig. 1 that is driven by Ekman pumping of the form $[1/f(y)]\sin[(y - b)\pi/\Delta]$ [see appendix, (A5)].

Over most of the subtropical gyre domain, these solutions are stable propagating waves. It is evident both visually and from the numerical integrations of the ray equations for k and l, shown in Fig. 3, that both families of waves are strongly refracted in the background flow so that wavenumber vectors initially specified at the eastern boundary bend from pointing nearly westward at the eastern boundary to pointing toward the northwest in the interior and, particularly for the A mode, greatly increase in length.

Integration of the ray equations is terminated when they begin to give complex valued solutions. The locus of points at which this occurs appears qualitatively to correspond to the edge of the unstable region visible in the southwest region of the subtropical gyre in the numerical solutions of Figs. 1 and 4 (see ray paths in Fig. 4). Integration of the ray equations for different initial values of l at the eastern boundary shows that the region of instability delineated in this manner is not the same for all solutions. Its extent is thus not defined by strictly local mean flow conditions, but rather depends on the scale of the incident waves. For the rather small range of eastern boundary wavenumbers l that, as noted above, are associated with Ekman pumping w'_E that is smooth at the meridional scale of the gyre, the variation is, however, not large. A region of westward amplification corresponding closely to the region of complex zonal wavenumbers fixed by integration of the ray equations appears in the southwestern subtropical gyre both in the wind-forced solution of Fig. 1 as well as in the A-mode and N-mode free wave solutions (Fig. 4 shows the N-mode solution). That this same region occurs in both the unforced free wave solutions of this section as well as in the everywhere forced solution of Fig. 1 suggests that spatial growth in the southwest corner of the gyre is excited by energy that has propagated westward into the region of spatial growth rather than by local forcing. This is borne out by numerical experiments (not shown) in which, although the forcing is restricted to the eastern one-third or one-quarter of the gyre, solutions farther west (including the spatial growth in the southwest corner of the gyre) are virtually identical to the everywhere forced solutions of Fig. 1.

5. Discussion and conclusions

We have analyzed the propagation of long, baroclinic planetary waves through the shadow zone of a spatially varying subtropical gyre flow to understand how fixed frequency, long baroclinic planetary waves evolve when propagating through the spatially inhomogeneous subtropical gyre background flow and how they can become energized in the southwestern part of subtropical gyre. As noted in the introduction, closely related problems have been studied numerically by Liu (1999a),

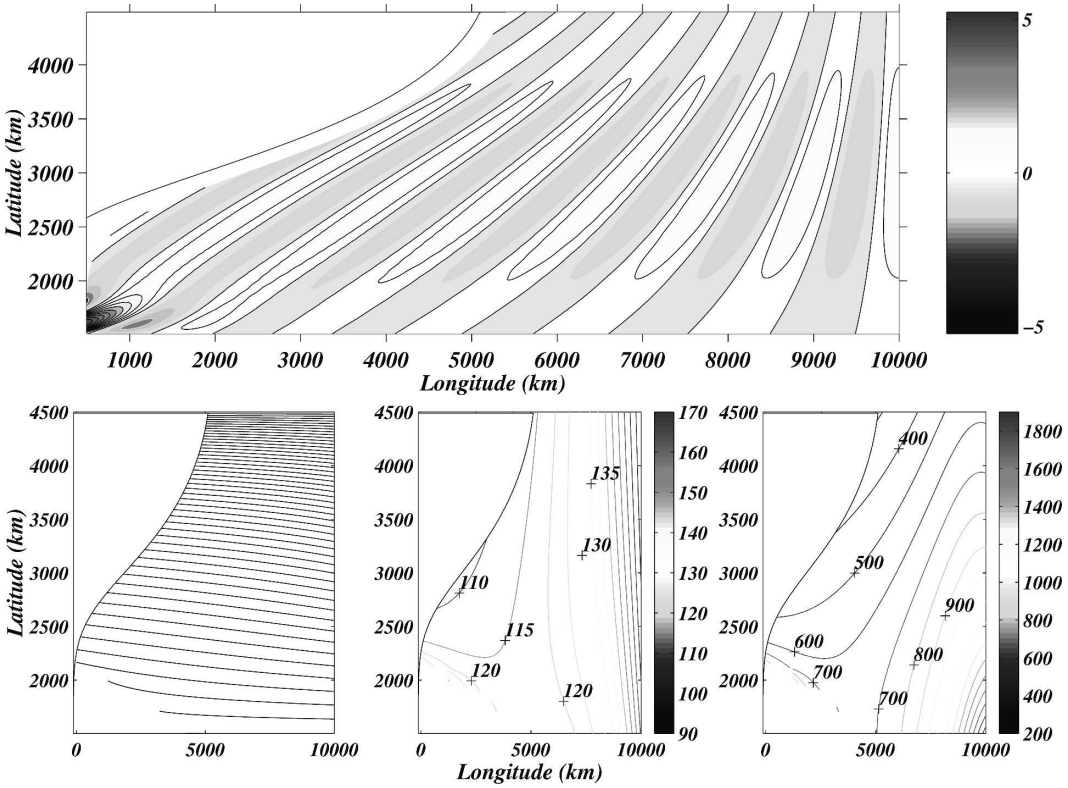

FIG. 4. (top) Snapshot of the N-mode time-variable interfacial displacement η_2 of the base of the middle layer obtained by solving (1) with no Ekman pumping but with specified values of η_1 and η_2 at the eastern boundary. There $\eta_2(y)$ is proportional to $\sin[(y - b)\pi/\Delta]$ (where b and Δ are the central latitude and the meridional extent of the basin) and $\eta_1(y)$ is given in terms of $\eta_2(y)$ by the equations in (1) and the dispersion relation (5). The solution is thus composed mainly of the meridional wavenumbers $l = \pm\pi/\Delta$ near the eastern boundary. The choice between the N-mode and the A-mode solution is made by choosing the corresponding root of the dispersion relation in evaluating $\eta_1(y)$ at the eastern boundary in terms of $\eta_2(y)$ there (the results are not sensitive to the choice of sign in $l = \pm\pi/\Delta$). The A-mode solution (not shown) is similar to the N-mode solution, except characterized by shorter wavelengths. Note (for both N-mode and A-mode solutions) the region of westward growth in the southwestern region of the gyre. (bottom from left to right) Ray paths $y(x)$, wavenumber direction $\tan^{-1}(l/k)$ (°), and wavelength $2\pi/(k^2 + l^2)^{1/2}$ (km) all obtained by solving ray equations for y and for the zonal and meridional wavenumbers k and l for the N-mode (long wave) solution of upper panel. Note that ray paths terminate (ray equations give complex values) at the edge of the region of growth in the solution of the upper panel and that wavelengths become large at the edge of this region.

Dewar (1998), and Dewar and Huang (2001), all of whom found instability only in the southwestern part of the subtropical gyre, whereas in contrast Walker and Pedlosky (2002) found that, with nonzero purely meridional background flow confined to the upper layer of a two-layer QG model, there was no minimum vertical shear required for instability, so instability need not be confined to any particular region of the subtropical gyre. This raises the question: why are baroclinically unstable solutions preferentially excited in the southwestern part of the subtropical gyre in numerical model results although there are possible unstable solutions everywhere in the basin?

The response in this paper is that, although the entire shadow zone of the model subtropical gyre with its nonzero meridional flow is potentially baroclinically unstable, over most of the shadow zone possibly unstable solutions are associated with meridional scales much smaller than those locally excited by Ekman pumping that is smooth at the meridional scale of the gyre. However, in the southwest corner of the shadow zone, refraction of waves generated farther eastward in the gyre by Ekman pumping, smooth at the meridional scale of the gyre, results in meridional scales small enough that the flow in the southwest corner of the gyre does become unstable. The region of instability is thus determined both by the meridional scales imposed by the Ekman pumping over the gyre and by the properties of the background subtropical gyre flow whose inhomogeneity causes refraction over the entire subtropical

gyre background flow, and not by a purely local property of the mean flow.

The large meridional scale of the time-periodic Ekman pumping in the present calculations thus plays an important role in the overall form of the solutions. The response of the real ocean to real Ekman pumping might be more complicated, both because the actual Ekman pumping field may have significant variability at scales smaller than the meridional scale of the gyre (e.g., Chelton et al. 2004), but also because the eastern boundary of the real ocean is not the straight meridional boundary of the present solutions but rather varies significantly over scales smaller than the meridional scale of the gyre.

Because ocean altimetry has been studied over a range of frequencies, from a fraction of a cycle per year to several cycles per year, it is important in attempting to relate the results of the present study to observations to understand how those results change as the frequency of the Ekman pumping is varied. It might be thought from study of the variation of the dispersion relation (5) with frequency that a change in frequency would greatly change the extent of the unstable region, yet solutions such as those in Figs. 1 and 4, but at frequencies from 0.25 to 2.0 cpy, show that the extent of the unstable region as measured by the occurrence of complex values in the ray-tracing calculation is remarkably independent of frequency: evidently refraction is so strong (Fig. 4) that scales sufficiently small for instability in the southwestern subtropical gyre are reached at about the same location in the gyre for a variety of interior scales. What does change with frequency, as expected from inspection of the dispersion relation (5), is the local growth rate. The 0.5-cpy counterpart of Fig. 1 shows much longer waves than for 1.0 cpy, as is expected from the dispersion relation, and no visible growth in the southwestern corner of the subtropical gyre, whereas the counterpart for 1.2 cpy shows appreciably shorter waves and greater growth.

The extent of the unstable region does of course increase as the background flow is strengthened. The mean flow of the present calculations is a gentle subtropical gyre, with a total western boundary current transport the order of 22 Sv ($\text{Sv} \equiv 10^6\ \text{m}^3\ \text{s}^{-1}$). Increasing the flow strength and transport (by increasing the strength of the steady Ekman pumping) increases the zonal extent of the unstable region. The present model is too schematic to support a detailed comparison of the extent of the unstable region with its counterpart, if any, in the real circulation, but it is appropriate to ask whether observations show anything like the model solution growth of time-periodic motions at and near the annual frequency in the southwestern subtropical gyre.

Chelton and Schlax (1996) found (i) well-defined westward propagation of features in the north subtropical Pacific Ocean altimetric sea level field bandpassed to include frequencies from 0.5 to 2 cpy accompanied by (ii) an increase in amplitude in the western half of the basin. Osychny and Cornillon (2004) found very similar results in the subtropical North Atlantic Ocean. The time–longitude plots at various latitudes of Chelton and Schlax (1996) are designed to facilitate the estimation of propagation speeds, but they were not intended to seek the sort of local amplification that occurs in the solutions of this paper in the southwestern corner of the gyre. The last is true of the frequency–zonal wavenumber spectra estimated by Osychny and Cornillon (2004) at a number of latitudes, even though those spectra are estimated separately eastward and westward of the mid-Atlantic Ridge. Osychny and Cornillon also map the Rossby wave amplitude in the period band from 4 years to 3 months, but their figure is dominated by the decay of variance away from the Gulf Stream and so does not clearly show spatial variation of sea level variance in the southwestern part of the North Altantic subtropical gyre.

Perhaps the strongest suggestion of amplification is provided by the 30 North Pacific high-resolution XBT transects analyzed in conjunction with simultaneous satellite altimetry by Roemmich and Gilson (2001). The transects go from San Francisco to Hawaii to Guam and finally to Taiwan or Hong Kong. A time–longitude plot of both SST and of the altimetry over the 7-yr (1993–99) extent of the XBT data clearly shows both (i) well-defined westward propagation of features that Roemmich and Gilson note are "the same features described by Chelton and Schlax (1996) as Rossby waves" as well as (ii) a striking increase in amplitude west of Hawaii. Their presentation of the rms variability of sea level from the altimetric data shows a clear maximum near to and eastward of the Kuroshio qualitatively similar to the maximum of Osychny and Cornillon (2004) near the Gulf Stream, as well as a strong secondary maximum at about 20°N extending eastward from the western boundary toward Hawaii.

A referee pointed out the work of Lin et al. (2005), who discuss baroclinic instability as a possible amplification mechanism for intraseasonal (180-day period) long Rossby waves in the subtropical ocean and show "wave amplification" areas in the north subtropical Pacific and Atlantic derived from Ocean Topography Experiment (TOPEX)/Poseidon altimetry. In the southwestern Pacific, the region thus identified falls in about the same latitude and latitude range as the maximum in the rms sea level variance of Roemmich and Gilson (2001).

Acknowledgments. This work was supported by the National Science Foundation through Grants OCE-9907008 and 0220471. IC would like to thank William Dewar for motivating and insightful discussions as well as two anonymous reviewers whose comments materially improved the paper.

APPENDIX

The Dynamical Model

The steady flow is modeled as in LPS. Three layers (upper, middle, and lower, labeled 1, 2, and 3, respectively) are considered. The depth of the lower layer will ultimately be allowed to become very large. The momentum balance is geostrophic,

$$-fv_j = -P_{jx} \quad \text{and} \quad fu_j = -P_{jy}, \tag{A1}$$

where subscripts x and y denote differentiation, u_j and v_j are horizontal fluid velocities in the zonal (x) and meridional (y) directions within layer j, and the Coriolis parameter f is linear in y; $f(y) = f_0 + \beta y$; $P_j = (p_j + \rho_j g z)/\rho_0$ is the Montgomery function, whose gradient depends only on the lateral position (x, y) within each layer, p_j is the true dynamic pressure in layer j, ρ_j is the (constant) density in the layer, and ρ_0 is a reference density. The vertical coordinate z is positive upward.

If H_j is the depth of the base of layer j, then the hydrostatic assumption causes the Montgomery function in layer j to be related to that in layer $j + 1$ by

$$P_j = \gamma_j H_j + P_{j+1}, \quad j = 1, 2, \tag{A2}$$

in which $\gamma_j = g(\rho_{j+1} - \rho_j)/\rho_0$, $j = 1, 2$, are reduced-gravity parameters. In terms of the layer thickness $h_j = H_j - H_{j-1}$, the mass conservation equation for layer j is

$$h_{jt} + J\left(P_j, \frac{h_j}{f}\right) = \begin{cases} -w_E, & \text{for} \quad j = 1 \\ 0, & \text{for} \quad j = 2, 3 \end{cases}, \tag{A3}$$

in which subscript t denotes the time derivative, J denotes the Jacobian $J(a, b) = -a_y b_x + a_x b_y$, and w_E is the wind-induced vertical velocity at the base of the surface Ekman layer. The sum of (A3) with constant H_3 gives the Sverdrup transport relation

$$-\frac{\beta}{f^2}\left(H_3 P_3 + \frac{1}{2}\gamma_1 H_1^2 + \frac{1}{2}\gamma_2 H_2^2\right)_x = -w_E. \tag{A4}$$

The steady flow occupies a midlatitude basin of zonal extent a and meridional extent Δ, and is driven by Ekman pumping of amplitude W_0 having the form

$$w_E^{(0)}(y) = -W_0\left(\frac{f_0}{f}\right)^2 \sin\left[\frac{(y-b)\pi}{\Delta}\right] \tag{A5}$$

in which f_0 is the Coriolis parameter at the central latitude $y = b$ of the basin. The steady Ekman pumping is chosen to be sufficiently weak that the deeper layers of the model never surface so that the steady flow occupies only the uppermost layer.

We study time-dependent perturbations linearized about the steady flow that are excited by harmonic forcing turned on at some initial time or by initial perturbations. We separate the variables into a steady part and time-dependent part as

$$P_j = P_j^0 + P_j', \quad w_E = w_E^0 + w_E',$$
$$H_1 = H_1^0 - \eta_1, \quad \text{and} \quad H_2 = H_2^0 - \eta_2. \tag{A6}$$

The perturbation mass conservation equations in (A3) for the middle and the lower layer become

$$\eta_{1t} - \eta_{2t} + J\left(P_3' - \gamma_2\eta_2, \frac{H_{20} - H_1^0}{f}\right) = 0 \tag{A7}$$

and

$$\eta_{2t} + J\left(P_3', \frac{H_{30} - H_{20}}{f}\right) = 0, \tag{A8}$$

where $H_2^0 = H_{20}$ is the depth of the bottom of the middle layer (constant when the steady flow in that layer is stagnant) and H_{30} is the flat bottom of the basin. The perturbation Sverdrup equation, obtained by integrating (A4) westward from the eastern boundary $x = a$ and linearizing about the steady flow, is

$$-\frac{\beta}{f^2}[H_{30}P_{3x}' - \gamma_1(H_1^0\eta_1)_x - \gamma_2 H_{20}\eta_{2x}] = -w_E'. \tag{A9}$$

We next reduce the model to two layers lying over an infinitely deep quiescent third layer to obtain the so-called 2½-layer model. From (A8), $P_3' \to 0$ as $H_{30} \to \infty$ so that (A7) becomes

$$\eta_{1t} - \eta_{2t} - J\left(\eta_2, \gamma_2\frac{H_{20} - H_1^0}{f}\right) = 0. \tag{A10}$$

We then solve the Sverdrup equation [(A9)] for P_3', insert the solution into (A8), and let the total depth $H_{30} \to \infty$, to obtain

$$\eta_{2t} - \frac{\beta\gamma_2 H_{20}}{f^2}\eta_{2x} - \frac{\beta\gamma_1}{f^2}(H_1^0\eta_1)_x = w_E'. \tag{A11}$$

Equations (A10) and (A11) constitute the 2½-layer model of the time-dependent perturbations η_1 and η_2 of nonzonal background flow.

REFERENCES

Barnier, B., 1988: A numerical study on the influence of the Mid-Atlantic Ridge on nonlinear first-mode baroclinic Rossby waves generated by seasonal winds. *J. Phys. Oceanogr.,* **18,** 417–433.

Cerovečki, I., and R. A. de Szoeke, 2006: Initially forced long planetary waves in the presence of nonzonal mean flow. *J. Phys. Oceanogr.,* **36,** 507–525.

Chelton, D. B., and M. G. Schlax, 1996: Global observations of oceanic Rossby waves. *Science,* **272,** 234–238.

——, M. Schlax, M. Freilich, and R. Millif, 2004: Satellite measurements reveal persistent small-scale features in ocean winds. *Science,* **303,** 978–983.

Dewar, W. K., 1998: On "too-fast" baroclinic planetary waves in the general circulation. *J. Phys. Oceanogr.,* **28,** 1739–1758.

——, and R. X. Huang, 2001: Adjustment of the ventilated thermocline. *J. Phys. Oceanogr.,* **31,** 1676–1697.

Gill, A. E., J. S. A. Green, and A. J. Simmons, 1974: Energy partition in the large-scale ocean circulation and the production of mid-ocean eddies. *Deep-Sea Res.,* **21,** 499–528.

Kubokawa, A., and M. Nagakura, 2002: Linear planetary wave dynamics in a 2.5-layer ventilated thermocline model. *J. Mar. Res.,* **60,** 367–404.

Lin, X., D. Wu, Q. Li, and J. Lan, 2005: An amplification mechanism of intraseasonal long Rossby wave in subtropical ocean. *J. Oceanogr.,* **61,** 369–378.

Liu, Z., 1999a: Planetary wave modes in the thermocline: Non-Doppler-shift mode, advective mode and Green mode. *Quart. J. Roy. Meteor. Soc.,* **125,** 1315–1339.

——, 1999b: Forced planetary wave response in a thermocline gyre. *J. Phys. Oceanogr.,* **29,** 1036–1055.

Luyten, J., J. Pedlosky, and H. Stommel, 1983: The ventilated thermocline. *J. Phys. Oceanogr.,* **13,** 293–309.

Osychny, V., and P. Cornillon, 2004: Properties of Rossby waves in the North Atlantic estimated from satellite data. *J. Phys. Oceanogr.,* **34,** 61–76.

Pedlosky, J., 1987: *Geophysical Fluid Dynamics.* 2d ed. Springer-Verlag, 710 pp.

——, 1989: Simple models for local instabilities in zonally inhomogeneous flows. *J. Atmos. Sci.,* **46,** 1769–1778.

Pierrehumbert, R. T., 1984: Local and global baroclinic instability of zonally varying flow. *J. Atmos. Sci.,* **41,** 2141–2162.

Roemmich, D., and J. Gilson, 2001: Eddy transport of heat and thermocline waters in the North Pacific: A key to interannual/decadal climate variability? *J. Phys. Oceanogr.,* **31,** 675–687.

Tailleux, R., and J. McWilliams, 2002: Energy propagation of long extratropical Rossby waves over slowly varying zonal topography. *J. Fluid Mech.,* **473,** 295–319.

Walker, A., and J. Pedlosky, 2002: Instability of meridional baroclinic currents. *J. Phys. Oceanogr.,* **32,** 1075–1093.